

Dynamin-related protein 1 deficiency accelerates lipopolysaccharide-induced acute liver injury and inflammation in mice

Lixiang Wang ^{1,2✉}, Xin Li³, Yuki Hanada ², Nao Hasuzawa⁴, Yoshinori Moriyama⁴, Masatoshi Nomura ^{2,4✉} & Ken Yamamoto ¹

Mitochondrial fusion and fission, which are strongly related to normal mitochondrial function, are referred to as mitochondrial dynamics. Mitochondrial fusion defects in the liver cause a non-alcoholic steatohepatitis-like phenotype and liver cancer. However, whether mitochondrial fission defect directly impair liver function and stimulate liver disease progression, too, is unclear. Dynamin-related protein 1 (DRP1) is a key factor controlling mitochondrial fission. We hypothesized that DRP1 defects are a causal factor directly involved in liver disease development and stimulate liver disease progression. Drp1 defects directly promoted endoplasmic reticulum (ER) stress, hepatocyte death, and subsequently induced infiltration of inflammatory macrophages. Drp1 deletion increased the expression of numerous genes involved in the immune response and DNA damage in *Drp1*LiKO mouse primary hepatocytes. We administered lipopolysaccharide (LPS) to liver-specific *Drp1*-knockout (*Drp1*LiKO) mice and observed an increased inflammatory cytokine expression in the liver and serum caused by exaggerated ER stress and enhanced inflammasome activation. This study indicates that Drp1 defect-induced mitochondrial dynamics dysfunction directly regulates the fate and function of hepatocytes and enhances LPS-induced acute liver injury in vivo.

¹Department of Medical Biochemistry, Kurume University School of Medicine, Kurume, Japan. ²Department of Medicine and Bioregulatory Science, Graduate School of Medical Science, Kyushu University, Higashi-ku, Fukuoka, Japan. ³Department of Molecular Pathobiology, New York University College of Dentistry, New York, NY, USA. ⁴Division of Endocrinology and Metabolism, Department of Internal Medicine, Kurume University School of Medicine, Kurume, Japan. ✉email: ourika0211@med.kurume-u.ac.jp; nomura@med.kurume-u.ac.jp

Mitochondria play a critical role in maintaining hepatocyte integrity and function, and mitochondrial dysfunction leads to liver diseases^{1–4}. Mitochondrial function and morphology are interdependent, and the latter is shaped by ongoing mitochondrial fusion and fission (mitochondrial dynamics)^{5–7}. In vertebrates, mitofusin-1/2 (MFN1/2) and optic atrophy 1 (OPA1) control mitochondrial fusion, while dynamin-related protein 1 (DRP1) and its receptors control mitochondrial fission. Mitochondrial dynamics research in recent years has shown the functional importance of mitochondrial dynamics in liver diseases. Kim et al. (2013, 2014) reported the impact of viral infection on mitochondrial dynamics, and mitochondrial dynamics alterations are used by hepatitis B virus⁸ and hepatitis C virus⁹ for maintenance of persistent infection. Overall, mitochondrial dynamics disruption promotes viral pathogenesis. Mitochondrial dynamics and liver diseases are at crossroads. Studies have reported abnormal mitochondrial dynamics in other liver pathophysiological conditions, too. Cadmium is a long-lived environmental and occupational pollutant, and cadmium hepatotoxicity induces DRP1-dependent mitochondrial fragmentation by disturbing calcium homeostasis¹⁰. Mitochondrial dynamics are also related to the mechanism underlying acetaminophen-induced acute liver damage. Acetaminophen changes mitochondrial DRP1 levels, and when the DRP1 inhibitor Mdivi-1 inhibits mitochondria fission, acetaminophen induces greater hepatic impairment¹¹. Alcoholic animal models also show mitochondrial morphology alteration. Mitochondria in normal hepatocytes usually show relatively slow dynamics, which are sensitive to inhibition by ethanol exposure¹². Mfn2 ablation in the liver causes endoplasmic reticulum (ER)-mitochondrial phosphatidylserine transfer defects, leading to a non-alcoholic steatohepatitis (NASH)-like phenotype and liver cancer¹³.

We reported that a mitochondrial fission defect in liver-specific *Drp1*-knockout (*Drp1*LiKO) mice, which demonstrate ER stress-promoted fibroblast growth factor 21 expression, subsequently functions as a metabolic regulator with anti-obesity and anti-diabetic effects. In addition, hematoxylin and eosin (H&E) staining of *Drp1*LiKO mouse liver sections shows a disorganized lobular parenchyma with inflammatory cell infiltration¹⁴. Our previous studies have also reported that *Drp1* disruption in the liver changes the expression of genes involved in the immune system in the liver. Gene Ontology (GO) biological studies have reported that 7 of the top 10 clusters are related to the immune system. These clusters include terms such as “immune response,” “phagocytosis,” “antigen processing,” and “presentation”¹⁵.

In this study, we hypothesized that *Drp1* deficiency-induced mitochondrial fission defects directly lead to liver disease development. In addition, we hypothesized that *Drp1* defects stimulate liver disease progression. The aim was to determine the relationship between mitochondrial fission defects and liver disease progression. We tested our hypotheses in an acute liver injury experimental mouse model via lipopolysaccharide (LPS)-induced endotoxin shock. Our study indicated that *Drp1* defect-induced liver inflammation progression, which will provide insight into the role of *Drp1* in liver function and acute liver injury.

Results

Increased inflammatory response and cell death in LPS-treated *Drp1*LiKO mice. In control mice, LPS administration increased messenger RNA (mRNA) levels of tumor necrosis factor alpha (*Tnfa*), interleukin 6 (*Il6*), interleukin 1 beta (*Il1b*), interferon beta 1 (*Ifnb1*), monocyte chemoattractant protein-1 (*Mcp1*), and the NLR family pyrin domain containing 3 (*Nlrp3*), which peaked at 1 h in the liver (Supplementary Fig. 1a). LPS-induced liver

TNF, IL-6, interleukin 10 (IL-10) and MCP1 levels peaked at 1 h, IL-1 β levels peaked at 4 h, and interferon gamma (IFN- γ) levels peaked at 8 h (Supplementary Fig. 1b). LPS-induced serum TNF and IL-10 levels peaked at 1 h; MCP1 level peaked at 4 h; and IL-6 and IFN- γ levels peaked at 8 h (Supplementary Fig. 1c).

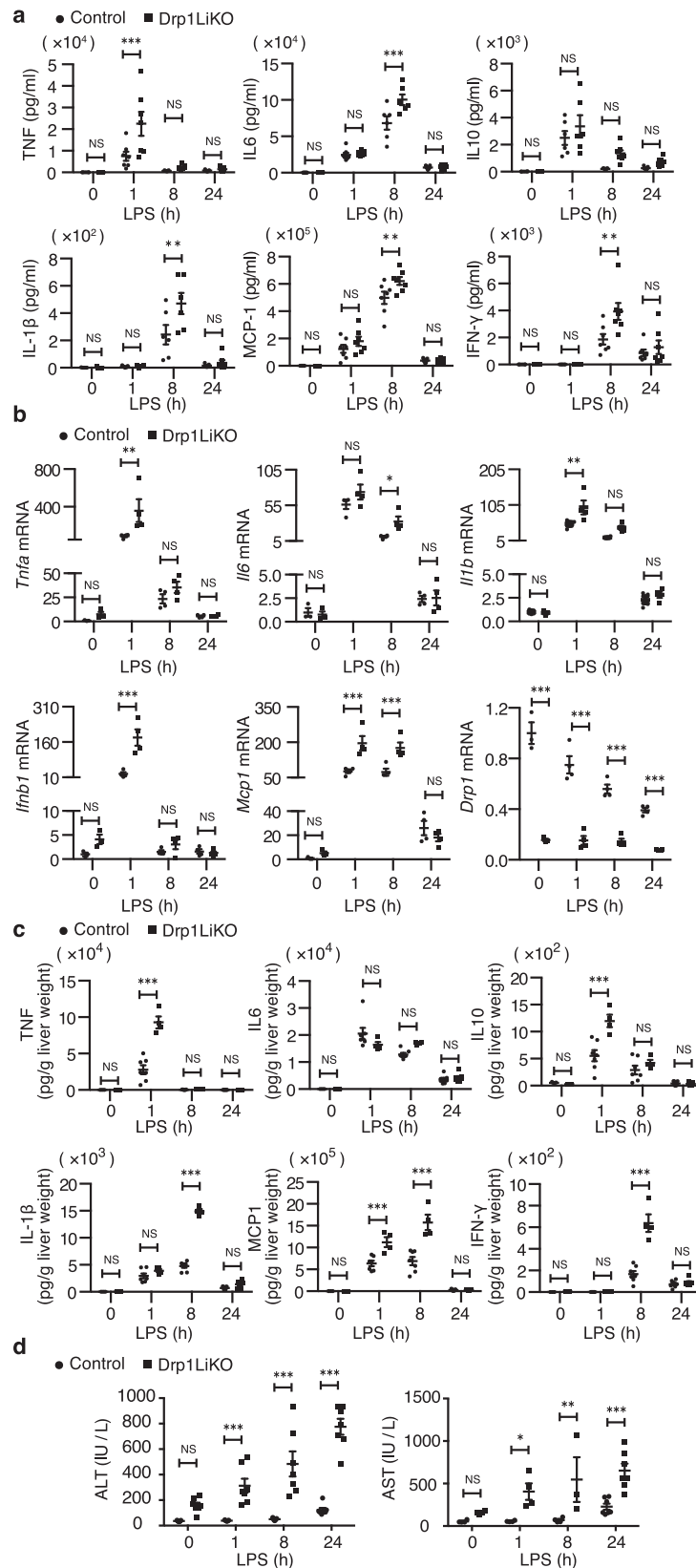
Next, we compared the responses to LPS in control and *Drp1*LiKO mice after LPS injection. *Drp1*LiKO mice developed more severe symptoms of endotoxin shock, such as lack of activity and hunched back posture. Consistent with this observation, we also observed a significant increase in serum TNF levels at 1 h and IL-6, IL-1 β , MCP1, and IFN- γ levels at 8 h after LPS injection in *Drp1*LiKO mice compared to control mice (Fig. 1a). In addition, liver *Tnfa*, *Il6*, *Il1b*, *Ifnb1*, and *Mcp1* mRNA expression levels also increased in LPS-treated *Drp1*LiKO mice compared to control mice. An interesting finding was a decrease in *Drp1* mRNA levels in control mice, probably through transcriptional inhibition (Fig. 1b). We also detected a significant increase in liver TNF, IL-10, IL-1 β , MCP1, and IFN- γ levels in LPS-treated *Drp1*LiKO mice (Fig. 1c).

To evaluate the degree of functional damage in the liver, we further analyzed the serum levels of alanine aminotransferase (ALT) and aspartate transaminase (AST), which are two markers of hepatocellular injury or necrosis. Both ALT and AST increased in LPS-treated *Drp1*LiKO mice (Fig. 1d), indicating increase of hepatocyte death in the absence of *Drp1*. Caspases are both initiators and effectors of apoptotic cascades¹⁶; we used western blot analysis to quantify the procaspase-3 and cleaved caspase-3 protein levels. We found that *Drp1* deletion increased cleaved caspase-3 levels in both non-treated and LPS-treated *Drp1*LiKO mice compared to control mice (Fig. 2a and b).

Increased ER stress response in LPS-treated *Drp1*LiKO mice.

Western blot analysis of the liver protein samples showed that LPS induces an inflammatory response via nuclear factor kappa B (NF- κ B) and mitogen-activated protein kinase (MAPK) pathways, while there was no difference in NF- κ B and MAPK pathways between control and *Drp1*LiKO mice (Supplementary Fig. 2a and b). In addition to these pathways, recent studies have reported that LPS promotes DRP1-dependent mitochondrial fission and associated inflammatory responses in different cell types^{17,18}. In the present study, LPS decreased *Drp1* mRNA levels in the liver (Fig. 1b); therefore, we examined LPS-regulated translational and post-translational modifications on DRP1. Phosphorylation of S616 (S635 in mice) and dephosphorylation of S637 (S656 in mice) are associated with the activation of DRP1 as well as its translocation to the mitochondria^{19–21}. First, we found that LPS induced a continuous decrease in *Drp1* protein levels in control mice (Fig. 2a and c); in contrast, LPS induced the robust phosphorylation of S635 at 1 h, indicating a transient increase in mitochondrial fission (Fig. 2a and d). *Drp1* phosphorylation levels of S656 were not detected.

It has previously been demonstrated that the ER stress pathway is involved in inflammatory responses and the pathogenesis of various chronic inflammatory diseases^{22–24}. In our previous study, we reported that *Drp1* deletion in the liver caused ER stress via the eukaryotic translation factor 2 α (P-eIF2 α) pathway¹⁴. Phosphorylation of eIF2 α levels increased in LPS-treated *Drp1*LiKO mice, indicating a further increase in ER stress in LPS-treated *Drp1*LiKO mice (Fig. 2a and e). ER stress evokes upregulation of activating transcription factor 3 (*Atf3*), DNA damage-inducible transcript 3 (*Ddit3*; *Chop*), nuclear protein 1 (*Nupr1*; *p8*), and Tribbles homolog 3 (*Trib3*), and these genes are related to ER stress and ER stress-mediated cell apoptosis^{25–27}. In the current study, real-time polymerase chain reaction (PCR) analysis confirmed that the



mRNA expression of these ER stress-related genes increased in LPS-treated *Drp1LiKO* mice livers (Fig. 2f).

Inflammasome overactivation in LPS-treated *Drp1LiKO* mice. Compared with control mice, western blot analysis showed that

LPS-treated *Drp1LiKO* mice increased the activation of NLRP3 inflammasome pathways during the LPS-induced inflammatory response in the liver as well as increased *Nlrp3* inflammasome marker IL-1 β and *Nlrp3* levels (Fig. 2g and h). Gasdermin D, a newly discovered intracellular protein, forming pores regulate the secretion of cytokines such as IL-1 β , in response to LPS and other

Fig. 1 LPS-induced inflammatory response was augmented in *Drp1*LiKO mice. Control and *Drp1*LiKO mice were treated with saline alone (referred to as LPS 0 h) or LPS (5 mg/kg, intraperitoneally). At indicated time points after LPS treatment, serum and liver samples were collected. **a** Serum TNF, IL-6, IL-10, IL-1 β , MCP1, and IFN- γ levels were determined by BD cytometric bead array. Values are expressed as mean \pm SEM. $n = 5-7$. $^{*}p < 0.01$, $^{***}p < 0.001$ determined by Two-way ANOVA with Bonferroni's Post Hoc Test. **b** Liver *Tnfa*, *Il6*, *Il1b*, *Ifnb1*, *Mcp1*, and *Drp1* mRNA expression was determined by quantitative real-time PCR. Results were normalized to *Gapdh* expression and are shown as fold-changes relative to gene expression in saline-treated control mice. Values are expressed as mean \pm SEM. $n = 3-4$ $^{*}p < 0.05$, $^{**}p < 0.01$, $^{***}p < 0.001$ determined by Two-way ANOVA with Bonferroni's Post Hoc Test. **c** Liver TNF, IL-6, IL-10, IL-1 β , MCP1 and IFN- γ levels were determined by the BD cytometric bead array. Values are expressed as mean \pm SEM. $n = 3-7$. $^{***}p < 0.001$ determined by Two-way ANOVA with Bonferroni's Post Hoc Test. **d** Serum ALT and AST levels were measured using the DRI-CHEM3500 Chemistry Analyzer. $n = 4-7$ $^{*}p < 0.05$, $^{**}p < 0.01$, $^{***}p < 0.001$ determined by Two-way ANOVA with Bonferroni's Post Hoc Test. LPS lipopolysaccharide; *Drp1*LiKO, liver-specific *Drp1*-knockout, TNF tumor necrosis factor, IL interleukin, MCP1 monocyte chemoattractant protein-1, IFN- γ interferon gamma, PCR polymerase chain reaction, *Gapdh* glyceraldehyde 3-phosphate dehydrogenase, ALT alanine aminotransferase, AST aspartate transaminase, SEM standard error of the mean, NS no significant difference.

activators of the inflammasome²⁸⁻³⁰. We also observed a significant increase in serum gasdermin D levels at 8 h and 24 h after LPS injection in *Drp1*LiKO mice compared to control mice (Fig. 2i). Macrophages represent a key cellular component of the liver and are essential for maintaining tissue homeostasis and ensuring rapid response to hepatic injury^{31,32}. Given that activation of the inflammasome pathway increased in *Drp1*LiKO mice, we investigated inflammasome activation in macrophages. To induce the maximum release of IL-1 β , mice received intraperitoneal injection of 10-mg/kg body weight LPS for 4 h and then an additional 50 μ l of 100-mM adenosine triphosphate (ATP) 30 min before sacrifice. H&E staining confirmed inflammatory cell infiltration in both saline- and LPS/ATP-treated livers of *Drp1*LiKO mice (Fig. 3a). Terminal deoxynucleotidyl transferase dUTP nick end labeling (TUNEL) staining showed that apoptotic hepatocytes increased in saline-treated (Ctrl 8.67 \pm 1.86 vs. KO 47.33 \pm 6.17) and LPS/ATP-treated (Ctrl 42.00 \pm 6.08 vs. KO 113.33 \pm 10.87) livers of *Drp1*LiKO mice (Fig. 3a and b). Consistent with this observation, serum ALT and AST levels also increased in LPS/ATP-treated *Drp1*LiKO mice (Supplementary Fig. 3a). Consistent with our previous observations (Fig. 1b), liver *Tnfa*, *Il6*, *Il1b*, *F4/80*, *Mcp1*, and *Nlrp3* mRNA expression significantly increased in *Drp1*LiKO mice compared to control mice after LPS/ATP treatment (Supplementary Fig. 3b).

Macrophages, neutrophils, T-cells, and B-cells are cell types known to play roles in liver inflammation; therefore, to determine the composition of inflammatory cell clusters in *Drp1*LiKO mice and especially the cell types that are predominantly expressed in these cell clusters, we performed immunostaining in liver tissues with various immune markers, including adhesion G protein-coupled receptor E1 (F4/80) for macrophages, lymphocyte antigen 6 complex, locus G (Ly6G) for neutrophils, CD3 antigen, epsilon polypeptide (CD3) for T-cells, and protein tyrosine phosphatase, receptor type, C (B220) for B-cells (Fig. 3a and Supplementary Fig. 4a). Cell-counting results are summarized in Fig. 3c and Supplementary Fig. 4b-d. We found no differences in the number of T-cells (Supplementary Fig. 4b) and neutrophils (Supplementary Fig. 4d), but the number of B-cells increased (saline Ctrl 183.33 \pm 26.64 vs. saline KO 367.00 \pm 22.50; LPS/ATP Ctrl 206.33 \pm 39.30 vs. LPS/ATP KO 382.33 \pm 29.85) (Supplementary Fig. 4c), and F4/80-positive macrophages were the largest population of the increased inflammatory cells (saline Ctrl 2401.50 \pm 243.40 vs. saline KO 6097.75 \pm 1089.91; LPS/ATP Ctrl 4851.25 \pm 167.44 vs. LPS/ATP KO 8630.50 \pm 904.51) (Fig. 3c). Interestingly, immunostaining analysis also revealed co-immunostaining of IL-1 β with F4/80-positive macrophages, indicating specific co-localization of IL-1 β -positive cells with macrophages (Fig. 3d and Supplementary Fig. 4e). We observed a clear line of liver-resident Kupffer cells along the sinusoid wall, which constituted the main macrophage population in the livers of control mice (Fig. 3d, dashed lines, Magnified1, 2, 5, and 6). In

contrast, macrophages in *Drp1*LiKO mice, showed an abnormal morphology with irregular location and distribution patterns, some macrophages with low F4/80 expression showed IL-1 β production even without LPS/ATP stimulation in *Drp1*LiKO mice but not in control mice (Fig. 3d, Magnified3 and Magnified4). In LPS/ATP treated *Drp1*LiKO mice, the majority of macrophages showed low F4/80 expression but high IL-1 β expression after LPS/ATP treatment (Fig. 3d, Magnified7), and only a few macrophages showed high F4/80 expression but no IL-1 β expression after LPS/ATP treatment (Fig. 3d, Magnified8).

It is possible that different populations of hepatic macrophages in control and *Drp1*LiKO mice exert distinct functions and contribute to differences in response to an acute LPS challenge. During acute inflammation, M1-polarized macrophages express high IL-1 β levels, while IL-1 β levels are undetectable in M2-polarized macrophages³³. To explore the polarization signature of these macrophages in the liver of control and *Drp1*LiKO mice, we performed a flow cytometry assay and sequential gating analysis using isolated non-parenchymal liver cells without LPS injection. Macrophages were identified as 7AAD⁻CD45⁺CD11b⁺F4/80⁺ cells (Fig. 3e), and the expression of the pro-inflammatory macrophage (M1) markers CD64 and CD80 as well as anti-inflammatory macrophage (M2) marker CD206 was used to verify polarization. Sequential gating analysis showed a significant increase in CD80^{High}CD64^{Lo}, CD80^{Lo}CD64^{High} and CD80^{High}CD64^{High} pro-inflammatory macrophages (Fig. 3f) but a decrease in CD206^{High} anti-inflammatory macrophages in *Drp1*LiKO mice (Fig. 3g). Therefore, *Drp1* loss in hepatocytes induces macrophage activation, and most of these activated macrophages are prone to differentiating into pro-inflammatory macrophages.

Decreased autophagy formation in LPS-treated *Drp1*LiKO mice. Autophagy is reported to be involved in mitochondrial dynamics and mitochondrial quality control; furthermore, autophagosomes are known to form at the mitochondria-ER contact site (MAM) in mammalian cells³⁴. In our previous study, we demonstrated that loss of *Drp1* leads to MAM defects; therefore, we investigated whether *Drp1* defects alter autophagy formation in LPS-treated hepatocytes. The autophagy pathways in the LPS-induced inflammatory response were activated, and the autophagy activation marker light chain 3-phospholipid-conjugated (LCLc3-II3-II) expression increased and peaked at 8 h after LPS treatment in control mice, while LCLc3-II3-II expression decreased in *Drp1*LiKO mice compared to control mice (Fig. 4a and b). It is known that the degradation of sequestosome 1 (SQSTM1/P62) by the autophagic-lysosome pathway and deficient autophagy can lead to P62 accumulation at the protein level^{35,36}. In addition, western blot analysis showed an increase in P62 accumulation in *Drp1*LiKO mice (Fig. 4a and c). Selective autophagy of mitochondria, known as mitophagy, is an important

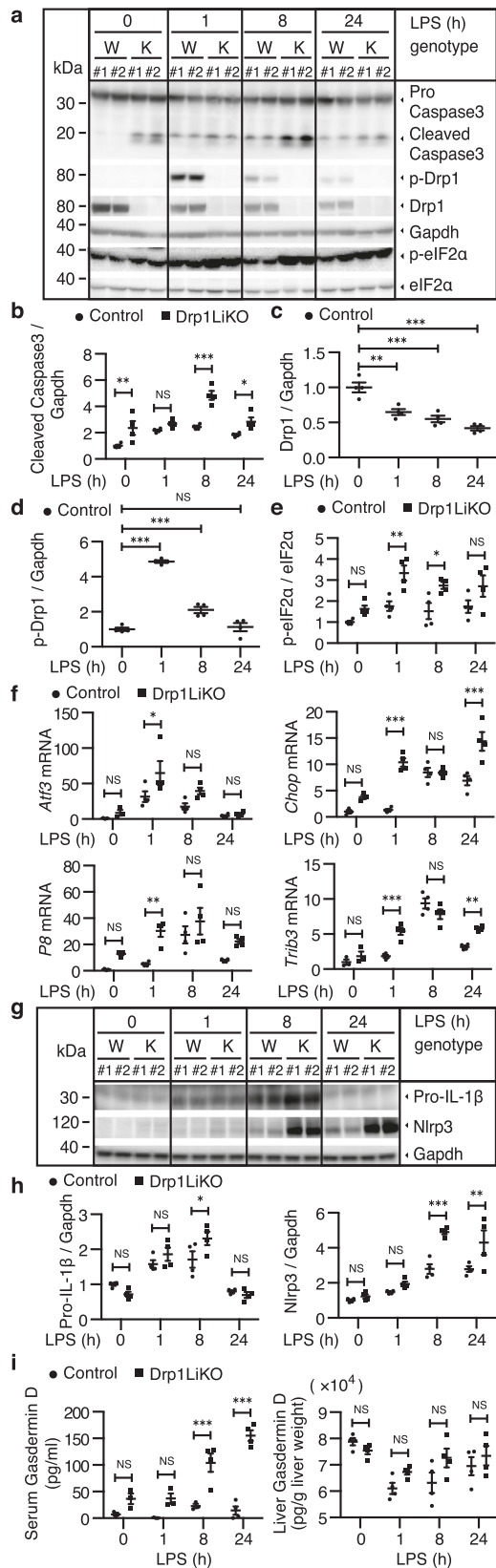


Fig. 2 LPS-induced increased ER stress and NLRP3 inflammasome activation in the liver of *Drp1LiKO* mice. Control and *Drp1LiKO* mice were treated with saline alone (referred to as LPS 0 h) or LPS (5 mg/kg, intraperitoneally). At indicated time points after LPS treatment, liver samples were collected. **a–e** Western blot analysis and densitometric quantification of caspase-3, p-Drp1(S635), Drp1, p-eIF2 α , and eIF2 α expression in saline- or LPS-treated liver lysates. Gapdh served as an internal control. The biological duplicate samples in each condition numbered as #1 and #2. Values are expressed as mean \pm SEM ($n = 4$). * $p < 0.05$, ** $p < 0.01$, and *** $p < 0.001$ determined by two-way ANOVA with Bonferroni’s post hoc test (**b** and **e**). ** $p < 0.01$ and *** $p < 0.001$ determined by one-way ANOVA with Dunnett’s multiple comparisons test (**c** and **d**). **f** Liver *Atf3*, *Chop*, *P8*, and *Trib3* mRNA expression were determined by quantitative real-time PCR. Results are normalized to *Gapdh* expression and are shown as fold-changes relative to gene expression in saline-treated control mice. Values are expressed as mean \pm SEM ($n = 3–4$). * $p < 0.05$, ** $p < 0.01$, and *** $p < 0.001$ determined by two-way ANOVA with Bonferroni’s post hoc test. **g, h** Western blot analysis and densitometric quantification of Pro-IL-1 β and Nlrp3 expression in saline- or LPS-treated liver lysates. Gapdh served as an internal control. The biological duplicate samples in each condition numbered as #1 and #2. Values are expressed as means \pm SEM ($n = 4$). * $p < 0.05$, ** $p < 0.01$, and *** $p < 0.001$ determined by two-way ANOVA with Bonferroni’s post hoc test. **i** Serum and liver gasdermin D levels were determined by Gasdermin D ELISA kit. Values are expressed as mean \pm SEM. $n = 3–4$. *** $p < 0.001$ determined by Two-way ANOVA with Bonferroni’s Post Hoc Test. LPS lipopolysaccharide, *Drp1LiKO* liver-specific *Drp1*-knockout, eIF2 α eukaryotic translation factor 2 α , *Atf3* activating transcription factor 3, *Chop* DNA damage-inducible transcript 3 (*Ddit3*), *P8* nuclear protein 1 (*Nupr1*), *Trib3* Tribbles homolog 3, NLRP3 NLR family pyrin domain containing 3, IL interleukin, *Gapdh* glyceraldehyde 3-phosphate dehydrogenase, PCR polymerase chain reaction, SEM standard error of the mean, NS no significant difference.

Drp1LiKO mice. There was a greater increase in Pink1 levels in *Drp1LiKO* mice at 1 and 8 h, which was sustained to 24 h after LPS treatment (Fig. 4a and d), indicating that LPS treatment induces mitophagy impairment and that mitophagy impairment is further disturbed by Drp1 defects in *Drp1LiKO* mice.

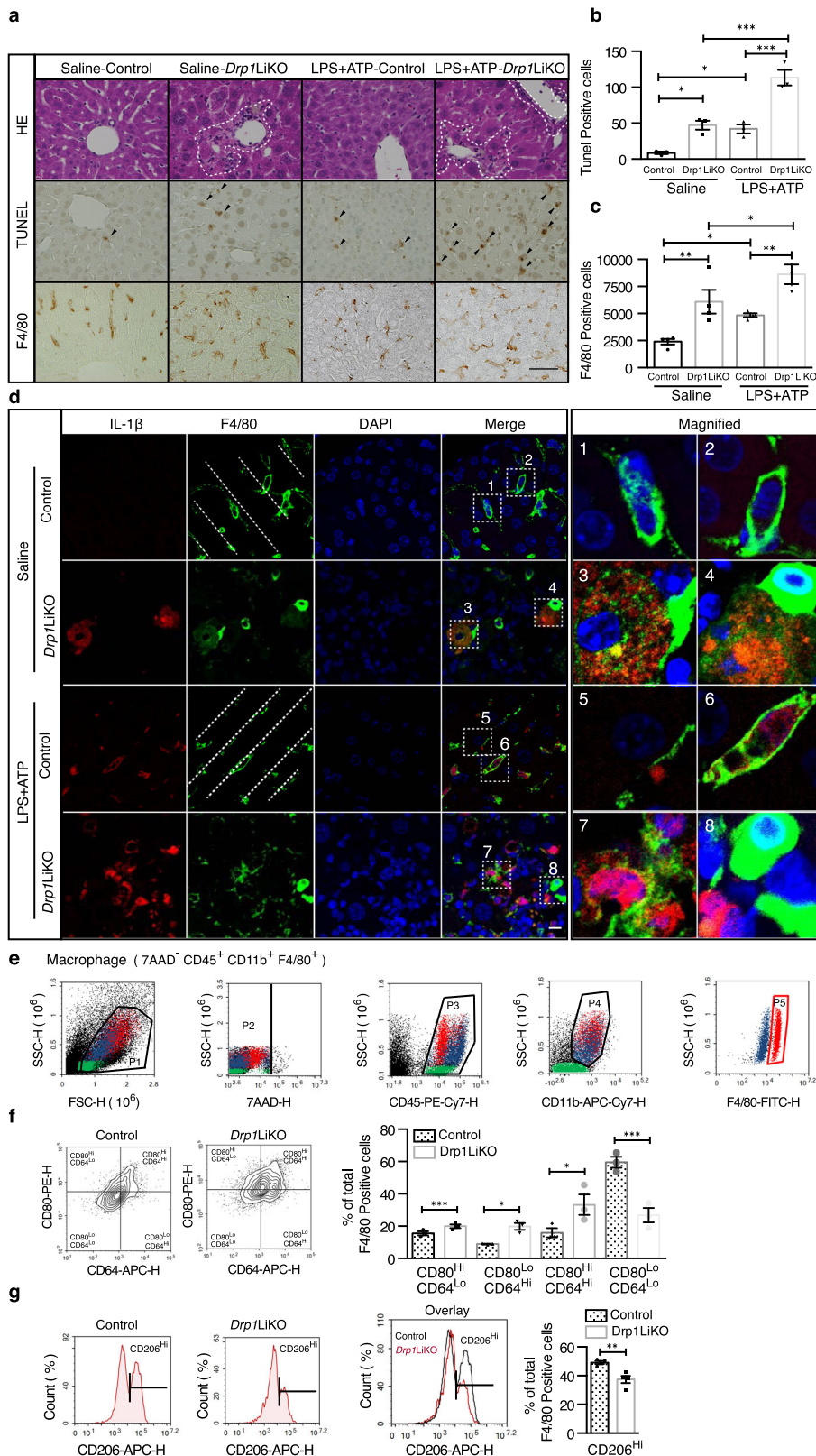
Immunofluorescence microscopy showed a decrease in LC3Lc3-II-positive dots in *Drp1LiKO* mice compared to control mice after LPS/ATP treatment (Fig. 4e). Of note, localization of LC3-Lc3-positive cells was different from that of IL-1 β -positive macrophages, indicating that autophagy occurs in hepatocytes but not in macrophages. Western blot analysis also confirmed that the LC3-ILc3-III in hepatocytes decreased in *Drp1LiKO* mice compared to control mice after LPS/ATP treatment (Fig. 4f).

Increased cell death, inflammatory response, and decreased $\Delta\Psi_m$ in *Drp1LiKO* mouse primary hepatocytes.

So far, our results showed that Drp1 disruption in the liver can lead to mitophagy defects and hepatocyte apoptosis, which might trigger enhanced infiltration and polarization of macrophages. To gain further insight into this mechanism, we conducted additional experiments with primary hepatocytes from control and *Drp1* knockout mice. Isolation and culture of the hepatocytes were performed using a two-step collagenase perfusion method. When examined and counted under a light microscope using a hemocytometer chamber, the cell yield and viability were less in *Drp1LiKO* mice compared to control mice, indicating that *Drp1* disruption in the liver impairs hepatocyte survival (Fig. 5a).

Next, to fully reveal the gene expression altered by *Drp1* deletion, we conducted an independent microarray analysis with primary hepatocyte harvested 24 h after seeding. Genes were selected using the criterion of a Z score of ≥ 2 , which identified

mitochondrial quality control mechanism³⁷. Phosphatase and tensin homolog-induced putative kinase 1 (PINK1) is an established mediator of mitophagy^{38–40}. In healthy mitochondria, which have a well-maintained mitochondrial membrane potential ($\Delta\Psi_m$), PINK1 levels remain low or undetectable. An acute LPS challenge led to Pink1 accumulation in both control and



680 upregulated and 559 downregulated genes in *Drp1*LiKO cells. We used the DAVID tool for functional clustering of upregulated and downregulated genes via similarly annotated GO biological process terms. The top five enriched annotation clusters of upregulated genes are shown in Fig. 5b. All five clusters for upregulated genes were related to the immune system: the immune system process, defense response to virus, innate

immune response, response to virus, and immune response. Genes involved in the immune system process are shown in Supplementary Table 1. The most significant five clusters for downregulated genes were related to mitotic nuclear division, cell cycle, cell division, chromosome segregation, and mitotic chromosome condensation. Genes involved in mitotic nuclear division are shown in Supplementary Table 2. These data are

Fig. 3 LPS/ATP-induced increased hepatocyte apoptosis and macrophage activation in *Drp1*LiKO mice. a-d Control and *Drp1*LiKO mice were treated with LPS (10 mg/kg body weight, intraperitoneally) for 4 h, followed by an additional 50 μ L intraperitoneally injection of 100 mM ATP 30 min before euthanization. H&E staining, TUNEL assay, and F4/80 immunostaining were performed on saline- or LPS/ATP-treated liver sections to examine histology (a). Areas with inflammatory cell infiltration are outlined by white dashed lines, and TUNEL-positive cells are indicated by arrowheads. Scale bar = 50 μ m. **b** Quantification of TUNEL-positive cells in saline- or LPS/ATP-treated control and *Drp1*LiKO mice. Values are expressed as mean \pm SEM. $n = 3$. * $p < 0.05$, *** $p < 0.001$ determined by Two-way ANOVA with Tukey's Post Hoc Test. **c** Quantitative analysis of the number of F4/80-positive cells performed by counting cells in 15 high-power fields (20 \times) per slide from 4 mice per group. Values are expressed as mean \pm SEM. $n = 4$. * $p < 0.05$, ** $p < 0.01$ determined by Two-way ANOVA with Tukey's Post Hoc Test. **d** Representative images of IL-1 β and F4/80 staining of liver tissue from saline- or LPS/ATP-treated mice. IL-1 β -positive cells were visualized using Alexa Fluor 594-conjugated chicken anti-goat IgG (red) and F4/80-positive cells using Alexa Fluor 488-conjugated rabbit anti-rat IgG (green). Nuclei were stained with DAPI (blue). Localization of Kupffer cells in the hepatic sinusoid is indicated (white dashed lines). Areas indicated with white dashed squares are enlarged and shown on the right side of the picture. Scale bar = 10 μ m. **e-g** *Drp1* ablation increases inflammatory macrophage infiltration in *Drp1*LiKO mice. **e** Gating strategy of macrophage (7AAD⁻CD45⁺CD11b⁺F4/80⁺). Cell populations were gated sequentially from left to right. **f** Flow cytometry representative images and percentage analysis of pro-inflammatory macrophages isolated from the liver tissue of normal chow diet-fed mice using inflammatory macrophage markers CD64 and CD80. Values are expressed as mean \pm SEM ($n = 3$). * $p < 0.05$ and *** $p < 0.001$ determined by an unpaired *t* test. **g** Flow cytometry representative images and percentage analysis of anti-inflammatory macrophages isolated from the liver tissue of normal chow diet-fed mice using anti-inflammatory macrophage marker CD206. Values are expressed as mean \pm SEM. $n = 4$. ** $p < 0.01$ determined by an unpaired *t* test. LPS lipopolysaccharide, ATP adenosine triphosphate, *Drp1*LiKO liver-specific *Drp1*-knockout, H&E hematoxylin and eosin, TUNEL terminal deoxynucleotidyl transferase dUTP nick end labeling, F4/80 adhesion G protein-coupled receptor E1, IL interleukin, DAPI 4',6-diamidino-2-phenylindole, SEM standard error of the mean, IgG immunoglobulin G.

consistent with previous studies that reported that DRP1 loss leads to cell arrest, replication stress, centrosome overduplication, and chromosomal instability, subsequently increasing DNA damage and cell apoptosis⁴¹. Overall, these findings showed that *Drp1* deletion increases the expression of numerous genes involved in the immune response and induces DNA damage in primary hepatocytes.

We further compared mitochondrial morphology using Mito Tracker Red, a specific mitochondria fluorescence probe (Fig. 5c). In control mouse primary hepatocytes, 57.17% \pm 4.00% of the mitochondria were fragmented, with only 14.80% \pm 2.35% hepatocytes showing tubular morphology. *Drp1*LiKO mouse primary hepatocytes containing fragmented mitochondria decreased to 10.50% \pm 2.66%, while those containing tubular mitochondria increased to 65.70% \pm 3.77% (Fig. 5d). These results indicated less mitochondrial fission and more mitochondrial fusion in *Drp1*LiKO mouse primary hepatocytes compared to control mouse primary hepatocytes.

The mitochondrial respiratory chain generates a membrane potential across the mitochondrial inner membrane as protons are pumped across the inner membrane. $\Delta\Psi_m$ regulates matrix configuration and cytochrome *c* release during apoptosis⁴². Tetramethylrhodamine ethyl ester (TMRE) accumulates in the mitochondrial matrix based on $\Delta\Psi_m$ (Fig. 5e); the percentage of hepatocytes showing collapse of $\Delta\Psi_m$ were increased in the *Drp1*LiKO hepatocyte compared to the control mouse primary hepatocyte culture (Ctrl 17.68% \pm 1.45% vs. KO 42.46% \pm 3.88%), indicating that *Drp1* defect induced the loss of $\Delta\Psi_m$ (Fig. 5f).

Decreased mitophagy formation and increased inflammatory response in LPS-treated *Drp1*LiKO mouse primary hepatocytes. We further performed in vitro studies in which mouse primary hepatocytes were treated with LPS. Optic atrophy 1 (OPA1) is a mitochondrial fusion protein that resides in the inner mitochondrial membrane; co-localization of OPA1 and LC3 indicates the sequestration of mitochondria inside autophagosomes. Co-localization of Opa1 and LC3Lc3 was barely observed in *Drp1*LiKO mouse primary hepatocytes (Fig. 6a); thus, we measured the co-localization frequency of Opa1 and LC3Lc3, and found that this co-localization frequency decreased in *Drp1*LiKO mouse primary hepatocytes, which confirmed our finding that *Drp1* defects induce mitophagy defects (Fig. 6b).

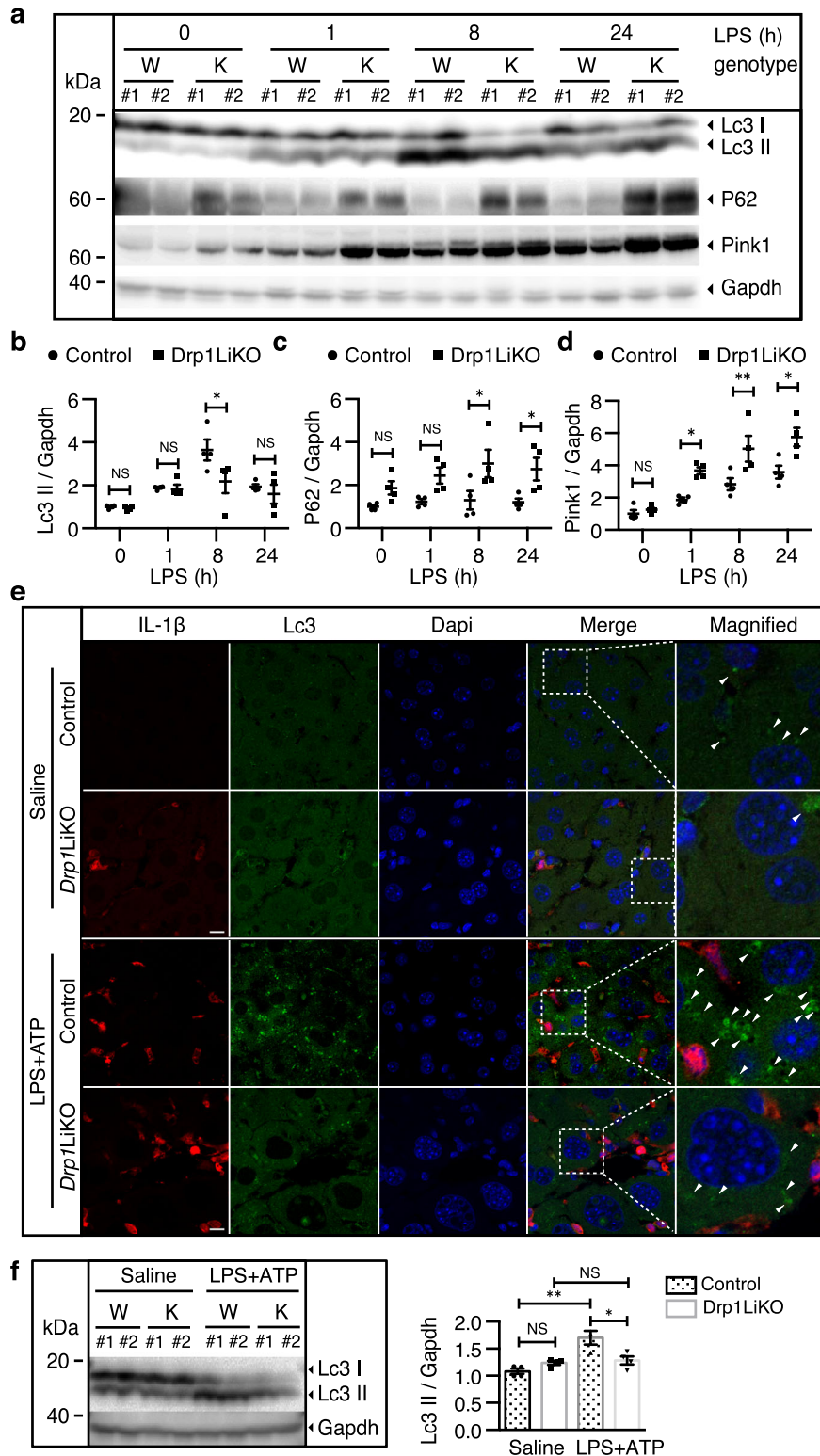
We found that LPS induced a decrease in phosphorylation of S635 at 4 h and 8 h, whereas total Drp1 protein levels were

unchanged in control mice (Fig. 6c and d). Phosphorylation of S635 emerged before LPS treatment, which might have been due to a metabolic effect, as mitochondria were shown to be short and fragmented in control primary hepatocytes incubated in sustained high glucose conditions (Fig. 5c). We also detected significantly increased TNF, IL-6, and IL-10 levels in *Drp1*LiKO hepatocyte culture supernatants (Fig. 6e). Consistent with these observations, we found a significant increase in *Tnfa*, *Il6*, and *Il1b* mRNA expression in *Drp1*LiKO mouse primary hepatocytes compared to control mouse primary hepatocytes (Fig. 6f).

ER stress induces an inflammatory response in *Drp1*LiKO mouse primary hepatocytes. To validate our results in mice, we used mouse primary hepatocytes to investigate whether *Drp1* deficiency induces inflammation through ER stress. We began by assessing the response to the well-known ER stress inducer thapsigargin. As thapsigargin concentration was increased, a dose-dependent increase in the expression of ER stress markers was observed; the expression of these markers was increased in thapsigargin-treated *Drp1*LiKO hepatocytes (Fig. 7a). Next, we compared the inflammatory responses to thapsigargin in control and *Drp1*LiKO hepatocytes. As expected, a significant increase in TNF and IL-6 protein levels was observed in the *Drp1*LiKO hepatocyte culture supernatant after thapsigargin treatment (Fig. 7b). Tauroursodeoxycholic acid (TUDCA) is an endogenous hydrophilic tertiary bile acid produces in humans at a low level. Mechanistic studies indicate that TUDCA prevents unfolded protein response dysfunction to attenuate ER stress⁴³. Recent studies have revealed that TUDCA, as a classic ER stress inhibitor, has an ameliorating effect on several diseases, including neurodegenerative diseases, biliary cirrhosis, and cholestatic liver diseases^{44,45}. We found that the mRNA expression levels of *Tnfa* and *Il6* were strongly inhibited by TUDCA treatment both in control and *Drp1*LiKO mouse primary hepatocytes (Fig. 7c). V-ZAD-FMK is a cell-permeable caspase inhibitor that has been shown to inhibit the induction of apoptosis^{46,47}. In the present study, treatment with V-ZAD-FMK also reduced the mRNA expression levels of *Tnfa* and *Il6* (Fig. 7c).

Discussion

Many studies have reported the abnormal function of mitochondrial dynamics in liver disease. Although mitochondrial fusion defects in the liver cause a NASH-like phenotype and liver



cancer, whether mitochondrial fission defects directly impair liver function and stimulate liver disease progression is unclear. In the present study, Drp1 defects led to elongated mitochondria with $\Delta\Psi_m$ collapse, mitophagy defect, DNA damage, and high expression of the ER stress-related genes *P8*, *Chop*, and *Trib3*. In turn, these changes increased hepatocyte death in *Drp1LiKO* mice and the dead hepatocytes released danger signals that led to inflammatory macrophage infiltration (Fig. 7d). Furthermore,

Drp1 loss in the liver led to an accelerated inflammatory response induced by LPS. Compared with control mice, *Drp1LiKO* mice showed increased expression of pro-inflammatory cytokines in the liver and serum, increased infiltration of inflammatory macrophages, enhanced inflammasome activation in the liver, increased hepatocyte apoptosis, and decreased mitophagy formation in hepatocytes. ER stress pathway protein-folding and quality control functions maintain cell homeostasis and are

Fig. 4 Drp1 defect decreased autophagy in *Drp1LiKO* mice. **a–d** Control and *Drp1LiKO* mice were treated with saline alone (referred to as LPS 0H) or LPS (5 mg/kg, intraperitoneally). At indicated time points after LPS treatment, liver tissue was collected. Liver Lc3, P62, and Pink1 levels were determined by western blot analysis. **b–d** Densitometric quantification of Lc3, P62, and Pink1 expression in saline- or LPS-treated liver lysates. Gapdh served as an internal control. The biological duplicate samples in each condition numbered as #1 and #2. Values are expressed as mean \pm SEM. $n = 4$. * $p < 0.05$, ** $p < 0.01$ determined by Two-way ANOVA with Bonferroni's Post Hoc Test. **e** Representative images of IL-1 β and Lc3 staining of liver tissue from LPS/ATPSaline- or LPS/ATP-treated mice. IL-1 β -positive cells were visualized using Alexa Fluor 594-conjugated chicken anti-goat IgG (red) and Lc3 positive cells using Alexa Fluor 488-conjugated donkey anti-rabbit IgG (green). Nuclei were stained with Dapi (blue). Areas indicated with white dashed squares are enlarged and shown on the right side of the picture. Arrowheads indicate Lc3-positive dots in hepatocytes. Scale bar = 10 μ m. **f** Western blot analysis of Lc3 and Gapdh expression in saline- or LPS/ATP-treated liver lysates. The bar graph shows the densitometric quantification of Lc3-II. Gapdh served as an internal control. The biological duplicate samples in each condition numbered as #1 and #2. Values are expressed as mean SEM. $n = 4$. * $p < 0.05$, ** $p < 0.01$ determined by Two-way ANOVA with Tukey's Post Hoc Test. *Drp1LiKO* liver-specific *Drp1*-knockout, LPS lipopolysaccharide, Sqstm1 sequestosome-1, Pink1 phosphatase and tensin homolog-induced putative kinase 1, Gapdh glyceraldehyde 3-phosphate dehydrogenase, IL interleukin, Lc3 light chain 3, ATP adenosine triphosphate, IgG immunoglobulin G, NS no significant difference, SEM standard error of the mean, Dapi 4',6-diamidino-2-phenylindole.

closely linked to mechanisms underlying immunity and inflammation^{25,48}. First, we found that exaggerated ER stress occurred in the LPS-treated liver of *Drp1LiKO* mice and in thapsigargin-treated *Drp1LiKO* mouse primary hepatocytes. Second, we found that the expression levels of inflammatory cytokines were increased as a direct consequence of this elevated ER stress response. Third, TUDCA treatment dramatically reduced the expression levels of inflammatory cytokines, exhibiting anti-inflammatory properties. Thus, the ER stress pathway is evoked in *Drp1LiKO* mice to promote hepatocyte apoptosis and liver inflammation.

Overall, these findings show that, upon an LPS challenge, exaggerated ER stress response in hepatocytes and NLRP3 inflammasome overactivation in inflammatory macrophages jointly contribute to the elevated inflammatory response observed in *Drp1LiKO* mice. Our study reveals that hepatocytes lacking DRP1 have an increased inflammatory response, whereas several recent studies have shown that a lack of DRP1 leads to lower inflammatory responses in macrophages and microglia^{17,18}. Hepatocytes and macrophages might be physiologically different in terms of DRP1-dependent apoptosis. Therefore, it will be worth studying and clarifying the function of DRP1 in apoptosis and inflammation according to cell type. In conclusion, using an acute liver injury experimental mouse model produced via LPS-induced endotoxin shock, we have presented approaches to studying DRP1 defect-induced liver inflammation progression that will provide insights into the role played by DRP1 in liver function and acute liver injury.

Drp1 deletion leads to the loss of $\Delta\Psi_m$ in *Drp1LiKO* mouse primary hepatocytes; since loss of $\Delta\Psi_m$ is closely linked to cell apoptosis by various insults, we believe that the increased population with $\Delta\Psi_m$ collapse in *Drp1LiKO* mouse primary hepatocytes might be an insult and/or a consequence induced by increased cell apoptosis. We have previously reported that, despite the observed morphological changes in mitochondria, the expression levels of the mitochondrial respiratory chain complex and mitochondrial respiratory activity were not changed by loss of DRP1¹⁴. Opening of the mitochondrial permeability transition pore (mPTP) causes inner membrane potential collapse and eventually leads to mitochondrial swelling, rupture, and cell death. In DRP1-deficient hearts and MEFs, inhibition of DRP1-mediated fission produces elongated mitochondria with increased mPTP opening⁴⁹. Furthermore, accelerated mPTP opening in DRP1 null mitochondria has been associated with mitophagy in MEFs and contributes to cardiomyocyte necrosis and dilated cardiomyopathy in mice⁵⁰. Mitochondrial outer membrane permeabilization (MOMP) also induces the loss of $\Delta\Psi_m$ and results in the release of apoptotic proteins that activate the downstream pathway of apoptosis. Although the mechanism by which DRP1 participates in MOMP remains to be elucidated, previous studies

indicate that DRP1 inhibition has direct effects on MOMP^{51,52} and that the role of DRP1 in MOMP can be distinguished from mitochondrial fission⁵³. Several studies have shown that $\Delta\Psi_m$ increases when mitophagy or autophagy are inhibited^{54–56}; nevertheless, it is possible to conclude that the increased population observed with $\Delta\Psi_m$ collapse in *Drp1LiKO* mouse primary hepatocytes may have been caused by mPTP opening and/or MOMP, which are independent of mitochondrial fission or mitophagy formation.

Mitochondrial dynamics and mitophagy have gained significant interest because these events modulate mitochondrial function during many physiological and pathological conditions. In a mouse embryonic fibroblast model, *Drp1* mutant cells showed abnormal mitochondrial morphology and defective mitophagy, leading to the activation of sterile myocardial inflammation, resulting in heart failure⁵⁷. In INS1 cells, inhibition of the fission machinery through a dominant-negative form of DRP1 (DRP1^{K38A}) decreases mitochondrial autophagy and results in the accumulation of damaged mitochondrial material⁵⁸. In a transverse aortic constriction mouse model, DRP1-dependent mitochondrial autophagy plays a protective role against pressure overload-induced mitochondrial dysfunction and heart failure⁵⁹. In addition, Parkin-independent mitophagy requires DRP1 and maintains the integrity of the mammalian heart and brain⁶⁰. Insufficient mitophagy formation induced by DRP1 defects might increase the inflammatory response and enhance the severity of liver injury in response to multiple pathogens.

Hepatitis, an inflammatory condition of the liver, is a serious global public health problem. Although it is usually caused by a viral infection, several other possible risk factors exist, including infections, alcohol, toxins, drugs, and autoimmune diseases. In this study, we demonstrated that mitochondrial fission defects caused by the lack of DRP1 lead to tissue damage associated with hepatitis, which suggests that DRP1 could be a therapeutic target for inflammatory liver disease. Under acute inflammatory liver disease, DRP1 could be potentially activated to restore a protective fission in hepatocytes. In recent years, lipid nanoparticles have been developed to passively and actively target drugs to the liver. Liver-targeted lipid nanoparticles with the expression of DRP1 or ablation of MFN2 by siRNA treatment (thereby inducing fission) could be used to produce anti-inflammatory activities. Overall, our study reveals that mitochondrial fission defects directly impair liver function and stimulate liver disease progression. Our examination of *Drp1LiKO* mice uncovered the essential role of mitochondrial fission in mitochondrial quality control for the prevention of hepatic inflammation. This exciting discovery offers a promising alternative approach to develop therapeutic strategies for the treatment of inflammatory liver disease.

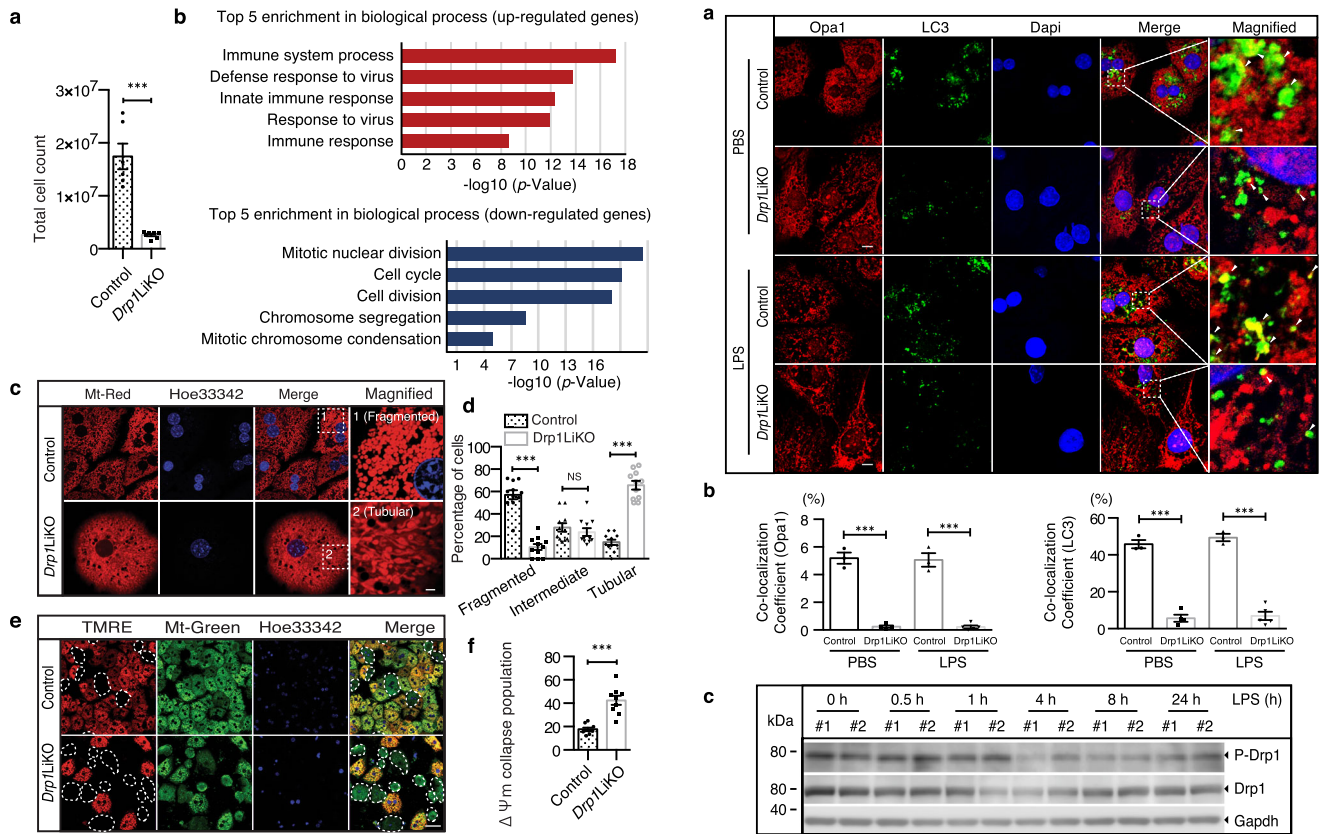
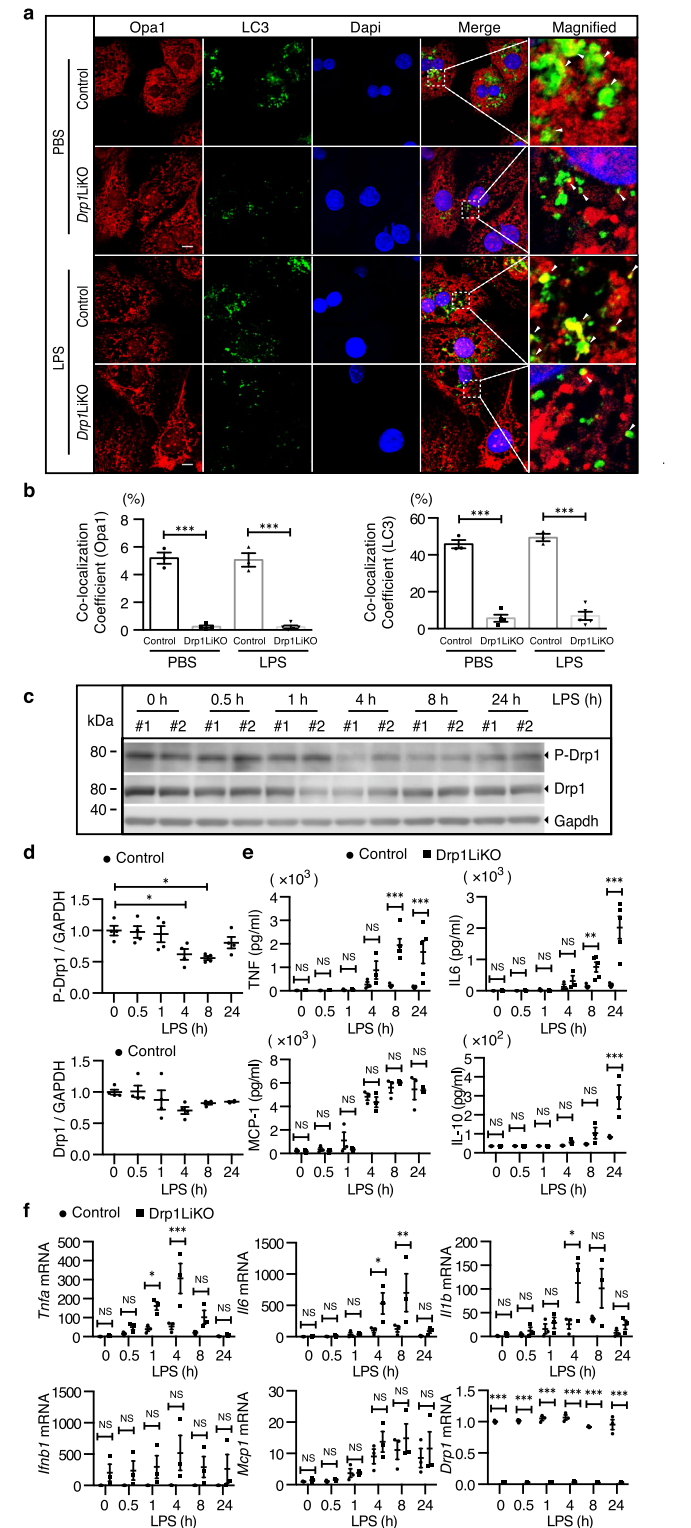


Fig. 5 Microarray functional annotation analysis, mitochondrial morphology, and mitochondrial membrane potential ($\Delta\Psi_m$) in control and *Drp1LiKO* mouse primary hepatocytes. **a** Total mouse primary hepatocyte numbers from control and *Drp1LiKO* mice were measured by trypan blue staining to measure viable cells. $n = 6-7$. $***p < 0.001$ determined by an unpaired *t* test. **b** Top five biological process GO terms of up- and down-regulated genes ranked by *p* value. **c, d** To visualize mitochondria, control and *Drp1LiKO* mouse primary hepatocytes were stained with MitoTracker® Red. Nuclei were stained with Hoechst33342, and images were captured with a confocal microscope. Areas indicated with white dashed squares are enlarged and shown on the right. Mitochondrial morphology was graded as fragmented, intermediate, or tubular for control and *Drp1LiKO* mouse primary hepatocytes. Quantification was performed by counting cells in 3–5 high-power fields (60 \times) per slide from three independent experiments. Scale bar = 10 μ m. $***p < 0.001$ determined by an unpaired *t* test. **e, f** Mitochondrial membrane potential ($\Delta\Psi_m$) measured in control and *Drp1LiKO* mouse primary hepatocytes using the fluorescence probe TMRE. Mitochondria and nuclei were stained by MitoTracker® Green and Hoechst33342, respectively. White dashed lines track cell boundaries with dissipated $\Delta\Psi_m$ (collapsed $\Delta\Psi_m$). Quantification of $\Delta\Psi_m$ collapse population was performed by counting cells in three high-power fields (20 \times) per slide from three independent experiments. Scale bar = 50 μ m. $***p < 0.001$ determined by an unpaired *t* test. *Drp1LiKO* liver-specific *Drp1*-knockout, SEM standard error of the mean, GO Gene Ontology, TMRE tetramethylrhodamine ethyl ester perchlorate.

Methods

Animals and reagents. We purchased 8–12-week-old male C57BL/6J mice from KBT Oriental Co., Ltd. (Saga, Japan). *Drp1LiKO* (*Alb-Cre^{Tg/+} Drp1^{lox/lox}*) and control (*Drp1^{lox/lox}*, sibling littermates) mice were generated by crossing *Drp1^{lox/+}* mice¹⁴ and *Alb-Cre* mice. The mice were maintained in a standard specific-pathogen free room at room temperature (22°C–24°C) and 50–60% relative humidity under a 12 h/12 h light/dark cycle (lights off at 8:00 p.m.). The mice were fed a normal chow diet (NCD; 5.4% fat, CRF-1; Orient Yeast, Tokyo, Japan) *ad libitum*. Experiments were performed between 10:00 and 11:00 a.m. after overnight fasting, except the LPS challenge and primary hepatocyte isolation (*ad libitum*). All

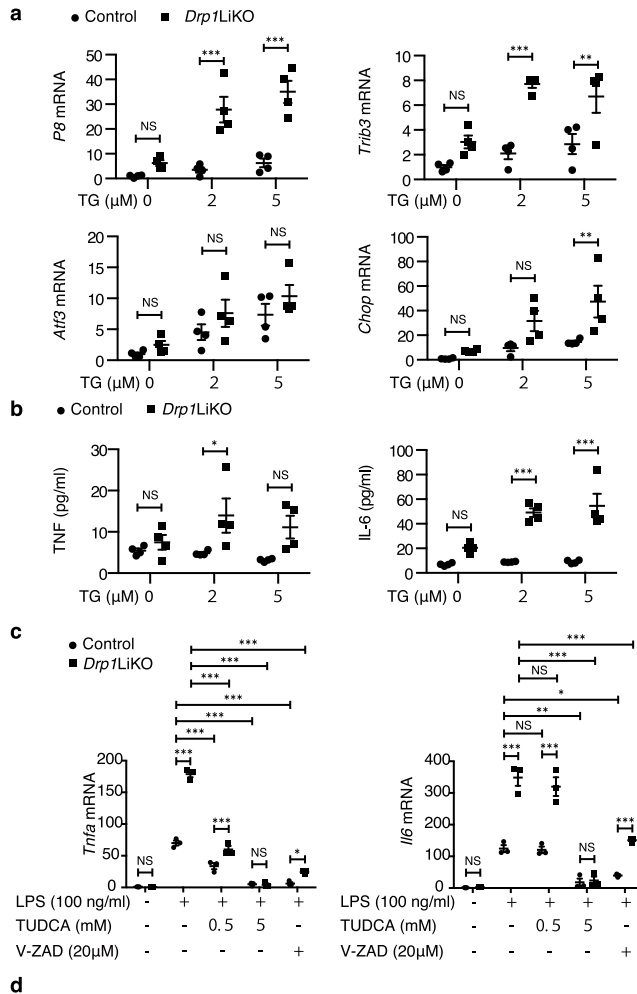


mouse procedures and protocols were approved by the Ethics Committees on Animal Experimentation (Kyushu University, Graduate School of Medicine, Japan) and performed in accordance with the Guide for the Care and Use of Laboratory Animals.

Reagents used in this study were listed in Supplementary Table 3.

Mouse primary hepatocyte isolation and culture. We performed a rapid two-step method⁵¹ to isolate mouse primary hepatocytes. We anesthetized the mice with pentobarbital sodium (50 mg/kg body weight) and perfused their liver tissue with prewarmed Hank's balanced salt solution supplemented with 0.5 mM ethylene glycol tetracetic acid (EGTA) and 10 mM 4-(2-hydroxyethyl)-1-piperazineethanesulfonic

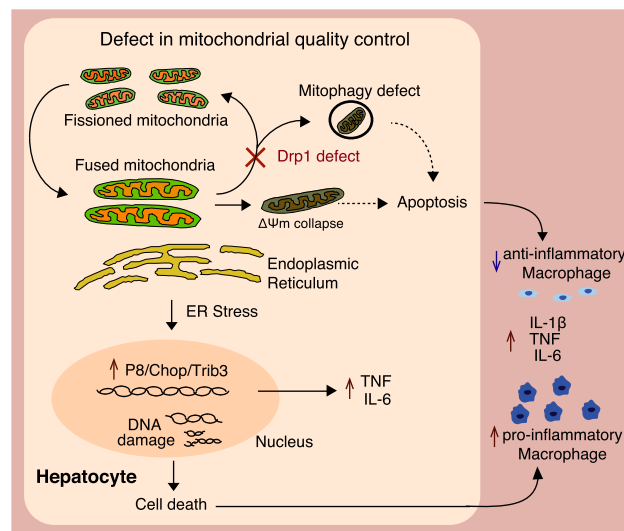
Fig. 6 Decreased mitophagy formation and increased inflammatory response induced by LPS treatment in *Drp1*LiKO mouse primary hepatocytes. Control and *Drp1*LiKO mouse primary hepatocytes were treated with PBS (referred to as LPS 0 h) or LPS (100 ng/ml). At indicated time points after LPS treatment, cells and culture supernatants were collected. **a** Representative images of Opa1 and Lc3 staining of PBS or LPS-treated (24 h) control and *Drp1*LiKO mouse primary hepatocytes. Opa1-positive cells were visualized using Alexa Fluor 594-conjugated goat anti-mouse IgG (red) and Lc3-positive cells using Alexa Fluor 488-conjugated donkey anti-rabbit IgG (green). Nuclei were stained with Dapi (blue). Areas indicated with white dashed squares are enlarged and shown on the right side of the picture. Scale bar = 10 μ m. **b** Statistical analysis of the co-localization efficiency of Opa1 and Lc3 by using ZEN software. $n = 3$. $***p < 0.001$ determined by Two-way ANOVA with Tukey's Post Hoc Test. **c, d** Western blot analysis and densitometric quantification of p-Drp1(S635) and Drp1 in PBS or LPS-treated cells. *Gapdh* served as an internal control. The biological duplicate samples in each condition numbered as #1 and #2. Values are expressed as mean \pm SEM ($n = 4$). $*p < 0.05$ determined by one-way ANOVA with Dunnett's multiple comparisons test. **e** TNF, IL-6, MCP1, and IL-10 levels were determined using a BD cytometric bead array ($n = 3-5$). $**p < 0.01$ and $***p < 0.001$ determined by two-way ANOVA with Bonferroni's post hoc test. **f** Total RNA was isolated at indicated time points after LPS treatment, and *Tnfa*, *Il6*, *Il1b*, *Ifnb1*, *Mcp1*, and *Drp1* expression was determined by quantitative real-time PCR. Results are normalized to *Gapdh* expression and are shown as fold-changes relative to gene expression in untreated control cells. Values are expressed as mean \pm SEM ($n = 3$). $*p < 0.05$, $**p < 0.01$, and $***p < 0.001$ determined by two-way ANOVA with Bonferroni's post hoc test. *Drp1*LiKO liver-specific *Drp1*-knockout, LPS lipopolysaccharide, Opa1 optic atrophy 1, Lc3 light chain 3, IgG immunoglobulin G, Dapi 4',6-diamidino-2-phenylindole, IL interleukin, TNF tumor necrosis factor, MCP1 monocyte chemoattractant protein-1, IFN- γ interferon gamma, *Gapdh* glyceraldehyde 3-phosphate dehydrogenase, SEM standard error of the mean.



acid (HEPES) for 5 min, followed by digestion buffer (1000 mg/L of low-glucose Dulbecco's modified Eagle's medium [DMEM] supplemented with 0.8 mg/mL of collagenase type 1; Worthington Biochemical Corporation, Lakewood, NJ, USA). Next, we filtered single-cell suspensions through a 70- μ m cell strainer (BD Falcon, Bedford, MA, USA) and centrifuged them at 50 \times g for 1 min and collected the cell supernatants separately for the preparation of nonparenchymal cells, as described later. We washed the hepatocytes in the pellet twice, suspended them in 4500 mg/L of high-glucose DMEM supplemented with 1 μ M insulin, 2 mM L-glutamine, 10 IU/mL of penicillin, 10 IU/mL of streptomycin, and 10% fetal bovine serum, and seeded them on 6-well plastic plates coated with collagen type I (Cellmatrix type I-P, Nitta Gelatin, Osaka, Japan) at a density of 300,000 cells/well. After 4 h incubation in a 5% CO₂ incubator at 37°C, we changed the culture medium to discard floating unattached cells, and the growth medium was changed daily.

Mouse hepatic nonparenchymal cell isolation and flow cytometry. To further explore the polarization signature of macrophages in the liver of control and *Drp1*LiKO mice, we performed flow cytometry assay and sequential gating analysis using isolated nonparenchymal hepatocytes without LPS injection. We prepared hepatic nonparenchymal cell containing suspensions from the liver, as described before. The suspensions were centrifuged at 50 \times g for 5 min to remove the remaining hepatocytes, and the resulting cell suspensions were pelleted by centrifugation at 800 \times g for 5 min and resuspended in phosphate-buffered saline (PBS) supplemented with 5% bovine serum albumin. Next, we stained cells with appropriate antibodies (Supplementary Table 4) for 30 min on ice, washed them, and analyzed them using a NovoCyte flow cytometer (ACEA Biosciences, San Diego, CA, USA) and NovoExpress software.

Total RNA isolation, microarray procedures, and real-time-PCR. We isolated total RNA from the mouse liver and primary hepatocytes using TRIzol Reagent (Invitrogen Corporation, Carlsbad, CA, USA) and purified it using the SV Total RNA Isolation System (Promega Corporation, Madison, WI, USA) according to the manufacturer's instructions. For microarray analysis, we amplified complementary RNA (cRNA) and labeled it using the Low input Quick Amp Labeling Kit (Agilent Technologies, Santa Clara, CA, USA). Next, we hybridized the cRNA to a 60 K 60-mer oligomicroarray (SurePrint G3 Mouse Gene Expression



Microarray 8x60K v2; Agilent Technologies) according to the manufacturer's instructions.

For real-time-PCR assays, we converted 500 ng of total RNA into first-strand complementary DNA (cDNA) using the QuantiTect Reverse Transcription Kit (QIAGEN, Hilden, Germany) according to the manufacturer's instructions. Next, we used the cDNA for quantitative real-time PCR using the power 2 \times SYBR Green PCR Master Mix and monitored the process using an ABI Prism 7500 sequence detection system (Thermo Fisher Scientific, Rockford, IL, USA). Supplementary Table 5 lists the primer sequences of the selected genes. We normalized relative gene expression versus control to *Gapdh* expression.

Fig. 7 Increased inflammatory response was inhibited by TUDCA pre-treatment in *Drp1*LiKO mouse primary hepatocytes. **a, b** Thapsigargin induced an elevated ER stress response and an increased inflammatory response in *Drp1*LiKO mouse primary hepatocytes. Control and *Drp1*LiKO mouse primary hepatocytes were treated with PBS (referred to as TG 0 μ M) or Thapsigargin (2 or 5 μ M) for 24 h. **a** *Atf3*, *Chop*, *P8*, and *Trib3* mRNA expression were determined by quantitative real-time PCR. Results are normalized to *Gapdh* expression and are shown as fold-changes relative to gene expression in PBS-treated control hepatocytes. Values are expressed as mean \pm SEM ($n = 3-4$). $**p < 0.01$ and $***p < 0.001$ determined by two-way ANOVA with Sidak's multiple comparisons test. **b** Culture supernatants were collected and TNF and IL-6 were determined by ELISA. Values are expressed as mean \pm SEM ($n = 4$). $*p < 0.05$ and $***p < 0.001$ determined by two-way ANOVA with Sidak's multiple comparisons test. **c** Control and *Drp1*LiKO mouse primary hepatocytes were pre-treated with PBS (referred to as TUDCA 0 mM), TUDCA (0.5 or 5.0 mM) for 24 h, or V-ZAD-FMK (20 μ M) for 1 h, and then cells were treated with PBS (referred to as LPS -) or LPS (100 ng/ml) for 4 h. Total RNA was isolated and *Tnfa* and *Il6* expression was determined by quantitative real-time PCR. Results are normalized to *Gapdh* expression and are shown as fold-changes relative to gene expression in untreated control cells. Values are expressed as mean \pm SEM ($n = 3$). $**p < 0.01$ and $***p < 0.001$ determined by two-way ANOVA with Tukey's post hoc test. **d** Schematic model of liver inflammation in *Drp1*LiKO mice. *Atf3* activating transcription factor 3, *Chop* DNA damage-inducible transcript 3 (*Ddit3*), *P8* nuclear protein 1 (*Nupr1*), *Trib3* Tribbles homolog 3, TNF tumor necrosis factor, IL interleukin, PCR polymerase chain reaction, *Gapdh* glyceraldehyde 3-phosphate dehydrogenase, ER endoplasmic reticulum, *Drp1*LiKO liver-specific *Drp1*-knockout, LPS lipopolysaccharide.

Western blot analysis. We homogenized fresh mouse liver tissue in western lysis buffer (20 mM Tris-HCl pH 7.6, 150 mM NaCl, 2 mM ethylenediaminetetraacetic acid [EDTA], 0.5% NP40) containing protease and phosphatase inhibitor tablet (Roche Applied Science, Mannheim, Germany) and centrifuged it at 10,000 \times g for 5 min at 4 $^{\circ}$ C. We discarded the pellet and measured the protein content using a bicinchoninic acid (BCA) Protein Assay kit (Thermo Fisher Scientific). Next, the samples were mixed with Laemmli sample buffer (1:1; Bio-Rad, Hercules, CA, USA) and heated for 5 min at 95 $^{\circ}$ C. We performed sodium dodecyl sulfate polyacrylamide gel electrophoresis (SDS-PAGE) on an equal amount of protein from each sample, trans-blotted it on a polyvinylidene difluoride (PVDF) membrane, and subjected it to immunoblot assay with primary antibodies, followed by horseradish peroxidase (HRP)-linked secondary antibodies. Supplementary Table 4 lists the primary and secondary antibodies used. Finally, we visualized protein bands using the electrochemiluminescence (ECL) Western Blotting Detection System (GE Healthcare, Buckinghamshire, UK).

Histology, immunohistochemistry, and live-cell imaging. We fixed liver tissue and primary hepatocytes by immersion in 4% (w/v) paraformaldehyde (PFA) overnight at 4 $^{\circ}$ C, embedded the liver tissue in paraffin according to standard methods, and cut it into 5- μ m-thick sections. For H&E staining, we stained the paraffin sections with Mayer's hematoxylin solution for 5 min, followed by counterstaining with 0.5% (v/v) eosin alcohol solution for 2 min. For immunostaining, we diluted primary and secondary antibodies in Can Get Signal[™] Immunoreaction Enhancer Solutions A and B, respectively (Toyobo, Osaka, Japan). Supplementary Table 4 lists the primary and secondary antibodies used. Next, we analyzed hepatocyte apoptosis using the TUNEL assay kit (Burlington, Boston, MA, USA) according to the standard protocol. The tissue sections were analyzed under a BZ-8000 microscope (Keyence, Osaka, Japan) or a confocal microscope LSM700 (Zeiss, Oberkochen, Germany). The OPA1 and LC3 co-localization measurements were performed using ZEN software (Zeiss, Oberkochen, Germany) according to the manufacturer's instructions.

For live-cell imaging, we seeded hepatocytes on a type I-coated 35 mm glass-based dish (Iwaki, Tokyo, Japan) preloaded with MitoTracker[®] Red, a specific mitochondria fluorescence probe. We further measured $\Delta\Psi_m$ using a fluorescence probe tetramethylrhodamine ethyl ester perchlorate (TMRE). Next, we examined the hepatocytes under the confocal microscope LSM700 and analyzed image data using ZEN software (Zeiss, Oberkochen, Germany). A hepatocyte was judged to have fragmented mitochondria if <25% of the mitochondria visible had a length five times their width and tubular if >75% of the mitochondria had a length five times their width.

Measurement of cytokine levels in the liver, serum, and cell culture supernatants. LPS was injected intraperitoneally into mice at 5 mg/kg body weight, and liver and serum samples were collected from the inferior vena cava at different time points (0, 1, 4, 8, 24, and 48 h). The liver tissue was perfused with cold PBS through the portal vein and then chopped into 1-2 mm pieces. Next, we added 100 mg of liver tissue to 1 mL of cell lysis buffer (R&D System, Minneapolis, MN, USA) and homogenized it using a tissue homogenizer. Finally, we diluted liver, serum, and cell culture supernatant samples with known high protein concentrations at 1:50 using an assay diluent and quantified the levels of various types of cytokines using the BD cytometric bead array (CBA) Cytokine kit (Becton-Dickinson, Franklin Lakes, NJ, USA) and a NovoCyte flow cytometer (ACEA Biosciences, San Diego, CA, USA) and NovoExpress software.

Biochemical assays. To evaluate the degree of functional damage in the liver, we measured serum ALT and AST levels (two markers of hepatocellular injury or necrosis) using the DRI-CHEM3500 Chemistry Analyzer (Fujifilm, Tokyo, Japan).

Enzyme-linked immunosorbent assay. Primary mouse hepatocytes were treated with thapsigargin (final concentration: 2 or 5 μ M) and the culture supernatants were collected and centrifuged to remove nonadherent cells. The concentrations of mouse TNF (Ab208348; Abcam, Cambridge, MA) and mouse IL-6 (M6000B; R&D Systems, Inc., Minneapolis, MN) were determined according to manufacturer's instructions. The serum and liver gasdermin D levels were determined using Gasdermin D (mouse) ELISA Kit (AG-45B-0011-K101; AdipoGen Life Science, Switzerland) according to manufacturer's instructions.

Statistics and reproducibility. All data were expressed as the mean \pm standard error of the mean (SEM). Two-tailed Student's *t* test was performed to compare two groups using Microsoft Excel (Mac 201012 version 16.16.27; Microsoft Japan, Tokyo, Japan). Two-way analysis of variance (ANOVA) with Bonferroni's Post Hoc Test or Tukey's post hoc test or ordinary one-way ANOVA was performed to compare multiple groups using GraphPad Prism 6.0 software (GraphPad, San Diego, CA, USA). To detect an outlier, we performed Grubbs' test using a free statistical calculator (QuickCals, <http://www.graphpad.com/quickcalcs/>). Significance levels were set at $p < 0.05$, $p < 0.01$, and $p < 0.001$.

Reporting summary. Further information on research design is available in the Nature Research Reporting Summary linked to this article.

Data availability

The microarray data from this publication have been submitted to the Gene Expression Omnibus database [<http://www.ncbi.nlm.nih.gov/geo/>] with an assigned identifier [accession: GSE156982]. Source data generated or analyzed during this study are provided in Supplementary Data 1 (source data for graphs) and a Supplementary information file (Supplementary Figs. 1–4, Supplementary Tables 1–7 and uncropped western blot images). The data that support the findings of this study are available from the corresponding authors upon reasonable request. A reporting summary for this article is available as a supplementary information file.

Received: 23 September 2020; Accepted: 30 June 2021;

Published online: 21 July 2021

References

- Hassanein, T. & Frederick, T. Mitochondrial dysfunction in liver disease and organ transplantation. *Mitochondrion* **4**, 609–620 (2004).
- Grattagliano, I. et al. Mitochondria in chronic liver disease. *Curr. Drug Targets* **12**, 879–893 (2011).
- Begriffe, K., Massart, J., Robin, M. A., Bonnet, F. & Fromenty, B. Mitochondrial adaptations and dysfunctions in nonalcoholic fatty liver disease. *Hepatology* **58**, 1497–1507 (2013).
- Koliaki, C. et al. Adaptation of hepatic mitochondrial function in humans with non-alcoholic fatty liver is lost in steatohepatitis. *Cell Metab.* **21**, 739–746 (2015).
- Detmer, S. A. & Chan, D. C. Functions and dysfunctions of mitochondrial dynamics. *Nat. Rev. Mol. Cell Biol.* **8**, 870–879 (2007).
- Liesa, M. & Shirihai, O. S. Mitochondrial dynamics in the regulation of nutrient utilization and energy expenditure. *Cell Metab.* **17**, 491–506 (2013).
- Wai, T. & Langer, T. Mitochondrial Dynamics and Metabolic Regulation. *Trends Endocrinol. Metab.* **27**, 105–117 (2016).
- Kim, S. J. et al. Hepatitis B virus disrupts mitochondrial dynamics: induces fission and mitophagy to attenuate apoptosis. *PLoS Pathog.* **9**, e1003722 (2013).

9. Kim, S. J. et al. Hepatitis C virus triggers mitochondrial fission and attenuates apoptosis to promote viral persistence. *Proc. Natl. Acad. Sci. USA* **111**, 6413–6418 (2014).
10. Xu, S. et al. Cadmium induced Drp1-dependent mitochondrial fragmentation by disturbing calcium homeostasis in its hepatotoxicity. *Cell Death Dis.* **4**, e540 (2013).
11. Gao, Y. et al. Early stage functions of mitochondrial autophagy and oxidative stress in acetaminophen-induced liver injury. *J. Cell Biochem* **118**, 3130–3141 (2017).
12. Das, S. et al. Mitochondrial morphology and dynamics in hepatocytes from normal and ethanol-fed rats. *Pflug. Arch.* **464**, 101–109 (2012).
13. Hernandez-Alvarez, M. I. et al. Deficient endoplasmic reticulum-mitochondrial phosphatidylserine transfer causes liver disease. *Cell* **177**, 881–895 e817 (2019).
14. Wang, L. et al. Disruption of mitochondrial fission in the liver protects mice from diet-induced obesity and metabolic deterioration. *Diabetologia* **58**, 2371–2380 (2015).
15. Wang, L. & Nomura, M. Loss of Drp1 in the liver leads to an alteration in expression of the genes involved in the immune system. *Genom. Data* **6**, 27–30 (2015).
16. Parrish, A. B., Freel, C. D. & Kornbluth, S. Cellular mechanisms controlling caspase activation and function. *Cold Spring Harb. Perspect Biol.* **5**, <https://doi.org/10.1101/cshperspect.a008672> (2013).
17. Kapetanovic, R. et al. Lipopolysaccharide promotes Drp1-dependent mitochondrial fission and associated inflammatory responses in macrophages. *Immunol. Cell Biol.* **98**, 528–539 (2020).
18. Nair, S. et al. Lipopolysaccharide-induced alteration of mitochondrial morphology induces a metabolic shift in microglia modulating the inflammatory response in vitro and in vivo. *Glia* **67**, 1047–1061 (2019).
19. Taguchi, N., Ishihara, N., Jofuku, A., Oka, T. & Mihara, K. Mitotic phosphorylation of dynamin-related GTPase Drp1 participates in mitochondrial fission. *J. Biol. Chem.* **282**, 11521–11529 (2007).
20. Cereghetti, G. M. et al. Dephosphorylation by calcineurin regulates translocation of Drp1 to mitochondria. *Proc. Natl. Acad. Sci. USA* **105**, 15803–15808 (2008).
21. Yu, X., Jia, L., Yu, W. & Du, H. Dephosphorylation by calcineurin regulates translocation of dynamin-related protein 1 to mitochondria in hepatic ischemia reperfusion induced hippocampus injury in young mice. *Brain Res.* **1711**, 68–76 (2019).
22. Hotamisligil, G. S. Endoplasmic reticulum stress and the inflammatory basis of metabolic disease. *Cell* **140**, 900–917 (2010).
23. McGuckin, M. A., Eri, R. D., Das, I., Lourie, R. & Florin, T. H. ER stress and the unfolded protein response in intestinal inflammation. *Am. J. Physiol. Gastrointest. Liver Physiol.* **298**, G820–G832 (2010).
24. Martinon, F. & Glimcher, L. H. Regulation of innate immunity by signaling pathways emerging from the endoplasmic reticulum. *Curr. Opin. Immunol.* **23**, 35–40 (2011).
25. Sano, R. & Reed, J. C. ER stress-induced cell death mechanisms. *Biochim Biophys. Acta* **1833**, 3460–3470 (2013).
26. Cai, D. et al. Nupr1/Chop signal axis is involved in mitochondrion-related endothelial cell apoptosis induced by methamphetamine. *Cell Death Dis.* **7**, e2161 (2016).
27. Ohoka, N., Yoshii, S., Hattori, T., Onozaki, K. & Hayashi, H. TRB3, a novel ER stress-inducible gene, is induced via ATF4-CHOP pathway and is involved in cell death. *EMBO J.* **24**, 1243–1255 (2005).
28. Rathkey, J. K. et al. Chemical disruption of the pyroptotic pore-forming protein gasdermin D inhibits inflammatory cell death and sepsis. *Sci. Immunol.* **3**, <https://doi.org/10.1126/sciimmunol.aat2738> (2018).
29. Liu, X. et al. Inflammasome-activated gasdermin D causes pyroptosis by forming membrane pores. *Nature* **535**, 153–158 (2016).
30. Evavold, C. L. et al. The pore-forming protein gasdermin d regulates interleukin-1 secretion from living macrophages. *Immunity* **48**, 35–44 e36 (2018).
31. Pelegrin, P. & Surprenant, A. Dynamics of macrophage polarization reveal new mechanism to inhibit IL-1 β release through pyrophosphates. *EMBO J.* **28**, 2114–2127 (2009).
32. Krenkel, O. & Tacke, F. Liver macrophages in tissue homeostasis and disease. *Nat. Rev. Immunol.* **17**, 306–321 (2017).
33. Ju, C. & Tacke, F. Hepatic macrophages in homeostasis and liver diseases: from pathogenesis to novel therapeutic strategies. *Cell Mol. Immunol.* **13**, 316–327 (2016).
34. Hamasaki, M. et al. Autophagosomes form at ER-mitochondria contact sites. *Nature* **495**, 389–393 (2013).
35. Watanabe, Y. & Tanaka, M. p62/SQSTM1 in autophagic clearance of a non-ubiquitylated substrate. *J. Cell Sci.* **124**, 2692–2701 (2011).
36. Komatsu, M. & Ichimura, Y. Physiological significance of selective degradation of p62 by autophagy. *FEBS Lett.* **584**, 1374–1378 (2010).
37. Ashrafi, G. & Schwarz, T. L. The pathways of mitophagy for quality control and clearance of mitochondria. *Cell Death Differ.* **20**, 31–42 (2013).
38. Narendra, D. P. et al. PINK1 is selectively stabilized on impaired mitochondria to activate Parkin. *PLoS Biol.* **8**, e1000298 (2010).
39. Geisler, S. et al. PINK1/Parkin-mediated mitophagy is dependent on VDAC1 and p62/SQSTM1. *Nat. Cell Biol.* **12**, 119–131 (2010).
40. Vives-Bauza, C. et al. PINK1-dependent recruitment of Parkin to mitochondria in mitophagy. *Proc. Natl. Acad. Sci. USA* **107**, 378–383 (2010).
41. Parone, P. A. et al. Preventing mitochondrial fission impairs mitochondrial function and leads to loss of mitochondrial DNA. *PLoS One* **3**, e3257 (2008).
42. Gottlieb, E., Armour, S. M., Harris, M. H. & Thompson, C. B. Mitochondrial membrane potential regulates matrix configuration and cytochrome c release during apoptosis. *Cell Death Differ.* **10**, 709–717 (2003).
43. Vang, S., Longley, K., Steer, C. J. & Low, W. C. The Unexpected Uses of Ursodeoxycholic Acid in the Treatment of Non-liver Diseases. *Glob. Adv. Health Med* **3**, 58–69 (2014).
44. Castro-Caldas, M. et al. Ursodeoxycholic acid prevents MPTP-induced dopaminergic cell death in a mouse model of Parkinson's disease. *Mol. Neurobiol.* **46**, 475–486 (2012).
45. Lindor, K. D. et al. Primary biliary cirrhosis. *Hepatology* **50**, 291–308 (2009).
46. Bossy-Wetzel, E., Newmeyer, D. D. & Green, D. R. Mitochondrial cytochrome c release in apoptosis occurs upstream of DEVD-specific caspase activation and independently of mitochondrial transmembrane depolarization. *EMBO J.* **17**, 37–49 (1998).
47. Gotttron, F. J., Ying, H. S. & Choi, D. W. Caspase inhibition selectively reduces the apoptotic component of oxygen-glucose deprivation-induced cortical neuronal cell death. *Mol. Cell Neurosci.* **9**, 159–169 (1997).
48. Chaudhari, N., Talwar, P., Parimisetty, A., Lefebvre d'Helencourt, C. & Ramanan, P. A molecular web: endoplasmic reticulum stress, inflammation, and oxidative stress. *Front Cell Neurosci.* **8**, 213 (2014).
49. Szabadkai, G. et al. Drp-1-dependent division of the mitochondrial network blocks intraorganellar Ca²⁺ waves and protects against Ca²⁺-mediated apoptosis. *Mol. Cell* **16**, 59–68 (2004).
50. Song, M., Mihara, K., Chen, Y., Scorrano, L. & Dorn, G. W. 2nd Mitochondrial fission and fusion factors reciprocally orchestrate mitophagic culling in mouse hearts and cultured fibroblasts. *Cell Metab.* **21**, 273–286 (2015).
51. Brooks, C. et al. Bak regulates mitochondrial morphology and pathology during apoptosis by interacting with mitofusins. *Proc. Natl. Acad. Sci. USA* **104**, 11649–11654 (2007).
52. Youle, R. J. & Karbowski, M. Mitochondrial fission in apoptosis. *Nat. Rev. Mol. Cell Biol.* **6**, 657–663 (2005).
53. Tanaka, A. & Youle, R. J. A chemical inhibitor of DRP1 uncouples mitochondrial fission and apoptosis. *Mol. Cell* **29**, 409–410 (2008).
54. Patoli, D. et al. Inhibition of mitophagy drives macrophage activation and antibacterial defense during sepsis. *J. Clin. Invest* **130**, 5858–5874 (2020).
55. Zhou, R., Yazdi, A. S., Menu, P. & Tschopp, J. A role for mitochondria in NLRP3 inflammasome activation. *Nature* **469**, 221–225 (2011).
56. Gomes, L. C., Di Benedetto, G. & Scorrano, L. During autophagy mitochondria elongate, are spared from degradation and sustain cell viability. *Nat. Cell Biol.* **13**, 589–598 (2011).
57. Cahill, T. J. et al. Resistance of dynamin-related protein 1 oligomers to disassembly impairs mitophagy, resulting in myocardial inflammation and heart failure. *J. Biol. Chem.* **290**, 25907–25919 (2015).
58. Twig, G. et al. Fission and selective fusion govern mitochondrial segregation and elimination by autophagy. *EMBO J.* **27**, 433–446 (2008).
59. Shirakabe, A. et al. Drp1-dependent mitochondrial autophagy plays a protective role against pressure overload-induced mitochondrial dysfunction and heart failure. *Circulation* **133**, 1249–1263 (2016).
60. Kageyama, Y. et al. Parkin-independent mitophagy requires Drp1 and maintains the integrity of mammalian heart and brain. *EMBO J.* **33**, 2798–2813 (2014).
61. Severgnini, M. et al. A rapid two-step method for isolation of functional primary mouse hepatocytes: cell characterization and asialoglycoprotein receptor based assay development. *Cytotechnology* **64**, 187–195 (2012).

Acknowledgements

We appreciate the technical assistance from The Research Support Center, Research Center for Human Disease modeling, Kyushu University Graduate School of Medical Sciences. This work was supported in part by the Japanese Society for the Promotion of Science (JSPS) KAKENHI (M. Nomura, Grant Number 23591356; L. Wang, Grant-in-Aid for Young Scientists B, Grant Number 16K19557).

Author contributions

L.W. and M.N. designed the experiments. L.W. performed the experiments. Y.H. and N.H. supported experiments. L.W. analyzed the data and wrote the manuscript. M.N., X.L., K.Y. and Y.M. supervised the analysis and edited the manuscript. M.N. and K.Y. are the guarantors of the article.

Competing interests

The authors declare no competing interests.

Additional information

Supplementary information The online version contains supplementary material available at <https://doi.org/10.1038/s42003-021-02413-6>.

Correspondence and requests for materials should be addressed to L.W. or M.N.

Peer review information *Communications Biology* thanks Charles Thomas and the other, anonymous, reviewer(s) for their contribution to the peer review of this work. Primary Handling Editors: Martina Rauner and Eve Rogers. Peer reviewer reports are available.

Reprints and permission information is available at <http://www.nature.com/reprints>

Publisher's note Springer Nature remains neutral with regard to jurisdictional claims in published maps and institutional affiliations.



Open Access This article is licensed under a Creative Commons Attribution 4.0 International License, which permits use, sharing, adaptation, distribution and reproduction in any medium or format, as long as you give appropriate credit to the original author(s) and the source, provide a link to the Creative Commons license, and indicate if changes were made. The images or other third party material in this article are included in the article's Creative Commons license, unless indicated otherwise in a credit line to the material. If material is not included in the article's Creative Commons license and your intended use is not permitted by statutory regulation or exceeds the permitted use, you will need to obtain permission directly from the copyright holder. To view a copy of this license, visit <http://creativecommons.org/licenses/by/4.0/>.

© The Author(s) 2021